Wastewater flocculation substrate derived three-dimensional ordered macroporous Co single-atom catalyst for singlet oxygen-dominated peroxymonosulfate activation

Xu Guo [a,b], Qicheng Zhang [a,b], Hongwei He [a,b], An Cai [a,b], Shibo Xi [c], Jiaqi Du [a,b], Fengbao Zhang [a,b], Xiaobin Fan [a,b], Wenchao Peng [a,b], Yang Li [a,b,*]

[a] *School of Chemical Engineering and Technology, Tianjin University, Tianjin 300354, China*
[b] *Institute of Shaoxing, Tianjin University, Zhejiang 312300, China*
[c] *Institute of Sustainability for Chemicals, Energy and Environment (ISCE2), Agency for Science, Technology and Research (A*STAR), 1 Pesek Road, Jurong Island 627833, Singapore*

ARTICLE INFO

ABSTRACT

Herein, wastewater flocculation substrate is used as a carbon source to prepare a three-dimensional ordered macroporous (3DOM) structure carbon-based catalyst with the Co—N$_4$ coordination active sites (Co-NC-PS) through a hard-template strategy. Abundant single-atom Co—N$_4$ active sites endow the Co-NC-PS with splendid performance in degrading organic pollutants by activating peroxymonosulfate (PMS). Experiment results show that the singlet oxygen ($^1O_2$) is the main reactive oxygen species (ROSs) for bisphenol A (BPA) degradation. The strong coordination of Co atoms with N atoms not merely avoids the leaching of Co and improves the stability of the catalyst but also establishes stable adsorption configuration and facilitates the generation of $^1O_2$ proven by density functional theory (DFT) calculations. This study provides the design of efficient Co carbon-based catalysts in mint conditions with high stability for water treatment, as well as a new idea for the preparation of high-value-added products from the recycling of flocculated waste.

1. Introduction

The water pollution caused by the discharge of industrial wastewater is frustrating worldwide and has become one of the urgent environmental problems [1,2]. Toxic substances in the discharged wastewater, such as dyes and phenols, are difficult to degrade naturally and are seriously harmful to human health [3–5]. Researchers have been developing adsorption, biodegradation, membrane separation, advanced oxidation processes (AOPs) and other methods to remove these organic pollutants [6–9]. Recently, AOPs based on peroxymonosulfate (PMS) have received extensive focus on account of the strong oxidizing ability of the generated reactive oxygen species (ROSs) [10]. The ROSs produced after PMS activation can mineralize various organic pollutants in a wide pH range with high reaction rates while generating minimal secondary pollution [11]. PMS can be activated by various methods, including heat treatment, microwaves, ultraviolet irradiation, ultrasonic treatment or transition metal catalysis [12–15]. Various transition metals, including Fe, Co, Cu, Ni, Mn and their oxides, are found to be able to activate PMS for generating ROSs [16]. Among them, the Co-based catalyst is one of the most effective catalysts to activate PMS due to the high standard reduction potential of Co^{3+}/Co^{2+} ($E^0 = 1.92$ V) [17,18]. However, the secondary pollution caused by Co leaching and limited catalytic stability greatly limits the practical application of Co-based catalysts [19]. Therefore, it is necessary to develop new Co-based catalysts with high stability and reusability.

Carbon materials have received extensive attention in heterogeneous catalysis due to their large specific surface area (SSA), adjustable physicochemical properties, and harmlessness [20,21]. Although N-doped carbon materials in the PMS-based AOPs show remarkable catalytic activity, the application of the non-metallic carbon materials is limited by their instability in a strongly oxidizing environment [22]. Decoration of transition metal onto carbon materials is an effective method to improve the catalytic activity and stability of the catalyst [23, 24]. In the past decade, carbon-based single-metal atom catalysts (SACs) have become at the forefront of heterogeneous catalysis [25,26]. For instance, Fei et al. reported an electrocatalyst for hydrogen generation

---

* Corresponding author.
  E-mail address: liyang1895@tju.edu.cn (Y. Li).

based on cobalt dispersed as individual atoms on nitrogen-doped graphene [27]. Liu et al. reported a high-performance electrocatalyst for H_2O_2 electrosynthesis consisting of atomically dispersed Co sites on N, P-codoped carbon substrate [28]. SACs have the advantages of high atomic utilization rate, excellent catalytic performance, high selectivity and good structural stability [29]. Many SACs are synthesized by pyrolysis of metal complexes or metal-organic frameworks [30]. However, these precursors are generally toxic, and manufacturing strategies are often complex and costly, making them impractical in environmental applications [31]. Thus, seeking inexpensive and environment-friendly substitutes as precursors is on the agenda.

Chitosan (CS) is a kind of abundant natural polymer biomass produced from the shell deacetylation of crustaceans. It has the advantages of wide sources, low cost and environmental friendliness [32]. CS, with abundant modifiable groups (e.g., amine group and hydroxyl group) in its backbone, has been widely used in chemical, pharmaceutical and environmental protection fields [33]. However, the flocculation substrate generated after the treatment by CS may give rise to secondary pollution [34]. Hence, researchers are also considering the recycling of such flocculated substrate [35].

Herein, novel research about the synthesis and catalytic application of Co single-atom catalyst (Co-NC-PS) fabricated through a sacrificial polystyrene microspheres template method, with the modified flocculation substrate as the precursor, is represented. Bisphenol A (BPA) is selected as the target pollutant to evaluate the PMS activation capability and stability of the obtained material. Comparing with template-free catalyst (Co-NC) and Co nanoparticles decorated carbon catalyst (NPs Co-NC-PS) are also evaluated, the Co-NS-PS catalyst with Co—N_4 coordination exhibits higher catalytic activity (1.290 min^{-1}), longer stability and better reusability. The singlet oxygen ($^1O_2$) is identified as the main active species for BPA degradation in the Co-NC-PS/PMS system. Moreover, density functional theory (DFT) calculation is used to investigate the process of PMS adsorption and activation by Co—N_4 active sites, as well as verifying the Co—N_4 active site is more inclined to transform PMS to $^1O_2$, rather than other ROSs. The reclamation of the flocculation substrate generated after the wastewater treatment provides new options for catalyst synthesis and thus may have great potential in the environmental fields.

2. Experimental section

2.1. Flocculation experiment

0.05 g methyl orange (MO) was dissolved in 1 L deionized water to obtain 50 mg·L^{-1} simulated MO dye wastewater. First, a certain amount of chitosan (0, 125, 180, 250, 375, 500 and 625 mg) was added to the simulated wastewater. Then, the pH of the solution was adjusted to a certain value (3, 4, 5, 6, 8, 9 and 10) with 0.1 M HCl or NaOH and stirred for 30 min. Finally, the flocculation substrate was obtained by standing for 8 h.

2.2. Synthesis of 3D ordered polystyrene (PS) microsphere template

The polystyrene (PS) microsphere template with a particle diameter of 350 nm was synthesized according to the following procedure. In a typical synthesis, 35 mL of styrene was washed thoroughly with 50 mL 0.1 M NaOH solution and deionized water successively to remove the stabilizer. 32.5 mL washed styrene and 500 mL deionized water were added to a triple-neck 1 L round-bottomed flask together. The mixture was heated at 90 ℃ under magnetic stirring for 30 min, bubbling with nitrogen. Then, 20 mL aqueous solution containing 0.31 g potassium persulfate was quickly added to the flask. After keeping stirring at a rotation rate of 300 rpm for 6 h at 90 ℃, the mixture was cooled down to room temperature and the obtained milk-like product was the monodispersed colloidal polystyrene microspheres.

2.3. Fabrication of flocculation substrate-derived catalysts

Firstly, 0.6 g glacial acetic acid was added to about 10 mL of liquid containing the flocculation substrate, followed by stirring in a 60 ℃ water bath for 30 min to dissolve. Next, 0.15 g melamine and 24 mg $CoCl_2$·6 H_2O were added to the above solution and stirred for 12 h to make it mixed thoroughly. The polystyrene microspheres were added into the emulsion according to the mass ratio of polystyrene microspheres to the flocculation substrate 8:1 and stirred for 12 h. After a 12 h frozen treatment, the ice content was removed entirely in a lyophilizer to obtain a light orange fluffy powder. Subsequently, the light orange powder was calcined for 2 h at 800 ℃ in N_2 atmosphere at a heating rate of 2 ℃·min^{-1}. The obtained black solid was ground and washed with HCl (0.5 M), stirring at room temperature for 12 h. Finally, the suspension was filtered and washed with deionized water to obtain Co-NC-PS. A series of catalysts with different loading amounts were obtained by changing the amount of Co source added, and the samples are named $Co_{(X)}$-NC-PS, where X represents the added mass (mg) of $CoCl_2$·6 H_2O in the above preparation process. In addition, a series of samples were obtained by changing the quantity of the polystyrene microspheres. The samples are named Co-NC-PS (Y:1), where Y represents the mass ratio of polystyrene microspheres to the flocculation substrate in the preparation process. The NC-PS sample was prepared in the same procedure without adding the cobalt source. For comparison, in the absence of the PS microsphere template or melamine, control samples were prepared according to the same procedure and named Co-NC and NPs Co-NC-PS, respectively.

3. Results and discussion

3.1. Synthesis and characterization of samples

Scheme 1 shows the two step-synthesis process of the Co single-atom catalyst. The first synthesis step is the flocculation of methyl orange (MO) simulated dye wastewater by chitosan (CS). The second synthesis step is the modification and calcination of the flocculation substrate to obtain 3DOM N-doped carbon Co-NC-PS. The effect of CS dosage and pH value on flocculation is investigated in the first synthesis step. The optimal dye removal rate can reach up to 88.9 % when CS dosage and flocculation pH are 250 mg and 5, respectively (Fig. S1a, S1b, S1c and S1d). The flocculation capacities of chitosan to different dyes have been investigated. Fig. S2 shows the flocculation of the four dyes at different pH. The optimal removal rate of Azo Rubine, New Coccine, Orange II and Brilliant Bule R can reach up to 99.9 % at pH = 6, 99.9 % at pH = 6, 99.8 % at pH = 5 % and 98.5 % at pH = 6, respectively. These results confirm that chitosan is an excellent flocculant for various dyes. In the second synthesis step, PS microspheres prepared by the soap-free emulsion method are used as a sacrificial template to obtain the 3DOM Co single-atom carbon material by the one-step calcination method. In that progress, PS microspheres decompose under high-temperature calcination [36].

The microstructure of the selected template strongly affects the morphology and pore structure of porous carbon. Scanning electron microscopy (SEM) confirms that the prepared PS microspheres are uniformly sized spheres with a diameter of ~360 nm (Fig. 1a and S3a). The PS microspheres with negative charge are used as structural templates to electrostatically bind with the positively charged CS polymer (carbon source) via protonated amine groups (Fig. S3b) [37]. During the subsequent pyrolysis process, the modified flocculating substrate is carbonized at 800 ℃ to form N-doped carbon sheets. Moreover, N atoms can anchor the Co atoms onto the carbon skeleton in the form of Co−N − C bonds [38]. SEM images also illustrate that the Co-NC-PS and NC-PS present almost the same 3DOM structures with abundant pores after high-temperature calcination (Figs. 1b, S3c and S3d), verifying the introduction of Co does not affect the morphology of the samples. The diameters of the pores are between 160 and 200 nm. The formed
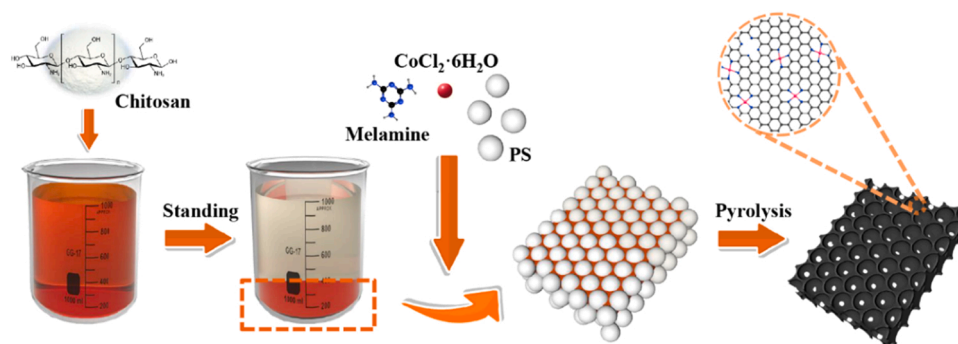
Scheme 1. The schematic diagram for the conversion of the flocculation substrate and the preparation of Co-NC-PS.
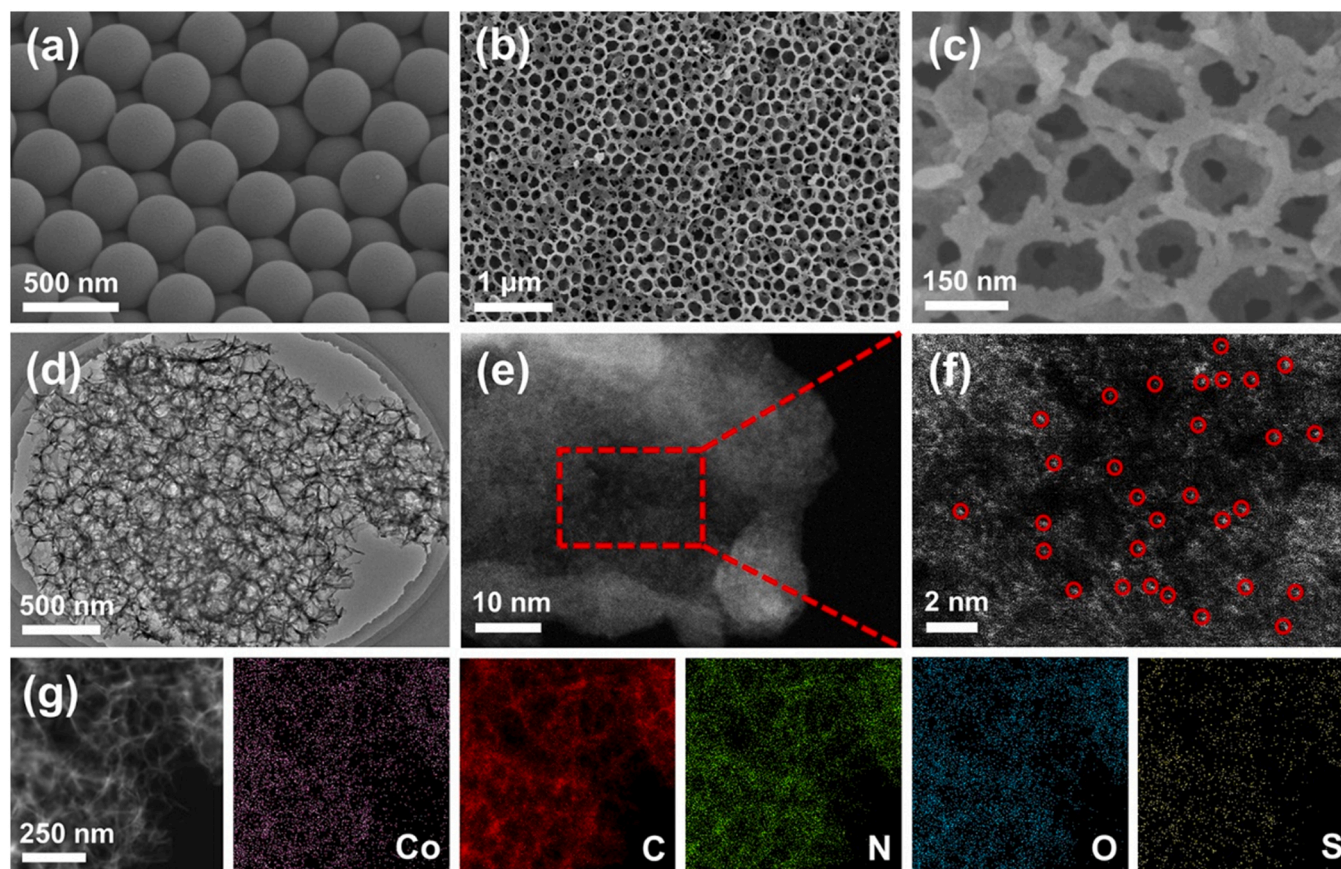

Fig. 1. (a) SEM image of PS microspheres. (b and c) SEM images and (d) TEM image of Co-NC-PS. (e and f) Aberration corrected the HAADF-STEM image, in which single Co atoms are highlighted by red circles. (g) HAADF-STEM image and corresponding EDS elemental mappings of Co, C, N, O and S, respectively.

macropores are smaller than the initial templates owing to the shrinkage of the melted PS spheres during calcination [39]. Moreover, the stacked PS microspheres are pyrolyzed to create rich interconnected pores (Fig. 1c). However, the Co-NC synthesized without the PS microsphere template possesses a massive structure without large pores (Fig. S3e). While the morphology and structure of the NPs Co-NC-PS without N source (Fig. S3f) are similar to those of the Co-NC-PS. The influence of the quantity of polystyrene microspheres on the morphology and pore structure of porous carbon is further investigated. The SEM image of Co-NC-PS (4:1) shows that some scattered holes appeared on the surface of the sample due to the removal of the polystyrene microspheres template (Fig. S4a). With the increased quantity of polystyrene microspheres, Co-NC-PS shows three-dimensional ordered macroporous (3DOM) structures with abundant pores (Fig. S4b). However, with the further addition of polystyrene microspheres, the SEM image of

Co-NC-PS (12:1) shows that the macropore structure collapses (Fig. S4c). The specific surface areas (SSAs) of the samples increase with the addition of polystyrene microspheres, which of the Co-NC, Co-NC-PS (4:1), Co-NC-PS and Co-NC-PS (12:1) are 33.4, 102.8, and 162.5 $m^2 \cdot g^{-1}$, respectively (Fig. S5a, S5c, S5e and S5g). Among them, Co-NC-PS contains more macropores, and its pore size distribution is concentrated in the range of $40 - 80$ nm (Fig. S5b, S5d, S5f and S5h). These results suggest that the PS microsphere template has a vital role in the formation of the 3DOM structure.

It can be clearly observed that the Co-NC-PS exhibits a three-dimensional hollow structure from the transmission electron microscopy (TEM) images (Fig. 1d). No clusters or nanoparticles are observed. Co atoms atomically dispersed in N-doped 3DOM carbon are verified by high-angle annular dark-field scanning transmission electron microscopy (HAADF-STEM) (Figs. 1e, 1f and 1g). Abundant Co single atoms

(bright dots, highlighted by circles) are uniformly dispersed on the carbon matrix. The corresponding energy dispersive X-ray spectroscopy (EDS) mappings (Fig. 1g) show that Co, C, N, O and S are uniformly distributed throughout the carbon skeleton. The existence of a small amount of S atoms in the obtained materials also confirms the effective utilization of organic constituents within the simulated MO dye wastewater.

In order to further detect the crystal state of C and Co, the X-ray diffraction (XRD) patterns of the samples are shown in Fig. 2a. XRD pattern of NC-PS only shows two wide diffraction peaks at 22° and 44°, corresponding to the (002) and (100) planes of graphite carbon. The XRD patterns of Co-NC, Co-NC-PS and Co$_{(X)}$-NC-PS samples are highly similar to that of NC-PS. The absence of a corresponding diffraction peak for the Co element suggests that Co-containing crystals may not be present (Fig. S6). Notably, the actual Co content in Co-NC-PS is determined by the Inductively Coupled Plasma Optical Emission Spectrometer (ICP-OES) to be 3.23 wt%. These results suggest that the Co elements may be atomically dispersed in the N-doped carbon preliminarily. The XRD pattern of NPs Co-NC-PS also shows two sharp narrow peaks at 44.2° and 51.4°, corresponding to the (111) and (200) facets of the metal Co, indicating the existence of cobalt particles. The graphitization degree and structural defects of all the above-mentioned samples are also investigated by Raman spectroscopy. The intensity ratio of the D band to the G band (I_D/I_G) usually represents the degree of structural defects of carbon-based materials [40,41]. As shown in Fig. 2b, the I_D/I_G of NC-PS, Co-NC and Co-NC-PS are 1.04, 1.04 and 1.05, respectively. It indicates that their defect degrees are almost the same. While the I_D/I_G of NPs Co-NC-PS is significantly smaller (0.96), which may be due to the fewer structural defects caused by the low degree N doping without melamine.

The above results preliminarily indicate that a kind of atomic Co anchored 3DOM structured carbon-based material has been prepared.

The introduction of the PS microsphere template does not change the crystalline state and defect degree of the carbon layer. The high dispersion of Co atoms in the Co-NC-PS sample benefits from the high defect degree and anchoring effect by abundant N dopant [42].

X-ray photoelectron spectroscopic (XPS) is employed to further investigate the surface composition and elemental state of the obtained materials. In the full range XPS spectrum of the Co-NC-PS (Fig. S7a), the signal of C, N, O and Co can be observed, while the signal of S is inconspicuous due to its low content (0.28 at%). XPS results show that the N, O and Co content of Co-NC-PS are 8.98, 5.98 and 0.35 at%, respectively. The Co 2p XPS spectrum of Co-NC-PS is shown in Fig. 2c. The characteristic peaks at 780.0 and 781.7 eV can be assigned to the Co^{3+} and Co^{2+} species [43]. No peak assigned to Co^0 is detected, suggesting all Co species in the Co-NC-PS exist in a dispersed oxidation state. The N 1 s high-resolution XPS spectra of NC-PS and Co-NC-PS are deconvolution into four peaks with binding energies of 398.5, 399.9, 401.1 and 403.3 eV, corresponding to pyridinic N, pyrrolic N, graphitic N and oxidized N, respectively (Fig. S7b and S7c) [40,44]. It is worth noting that the proportions of graphitic N in NC-PS and Co-NC-PS are 34.6 % and 30.8 %, as well as the proportions of pyridine N are 34.3 % and 39.4 %, respectively (Fig. 2d). The acceleration of the pyridine N ratio verifies the formation of Co-N coordination, as pyridine N is generally considered as anchoring sites for Co atoms [31].

The X-ray absorption near-edge structure (XANES) and extended X-ray absorption fine structure (EXAFS) are used to analyze the atomic coordination environment and valence information of Co-NC-PS. As shown in the inset in Fig. 3a, the first derivative of Co K-edge XANES spectra indicates that the absorption edge of Co-NC-PS is located between those of CoPc and Co$_3$O$_4$ [45–47]. This result suggests that the oxidation state of the Co element in Co-NC-PS is between + 2 ~ + 2.67, which is consistent with XPS results [48]. The k^2-weighted Fourier transform EXAFS (FT-EXAFS) spectrum of Co-NC-PS shows a major peak
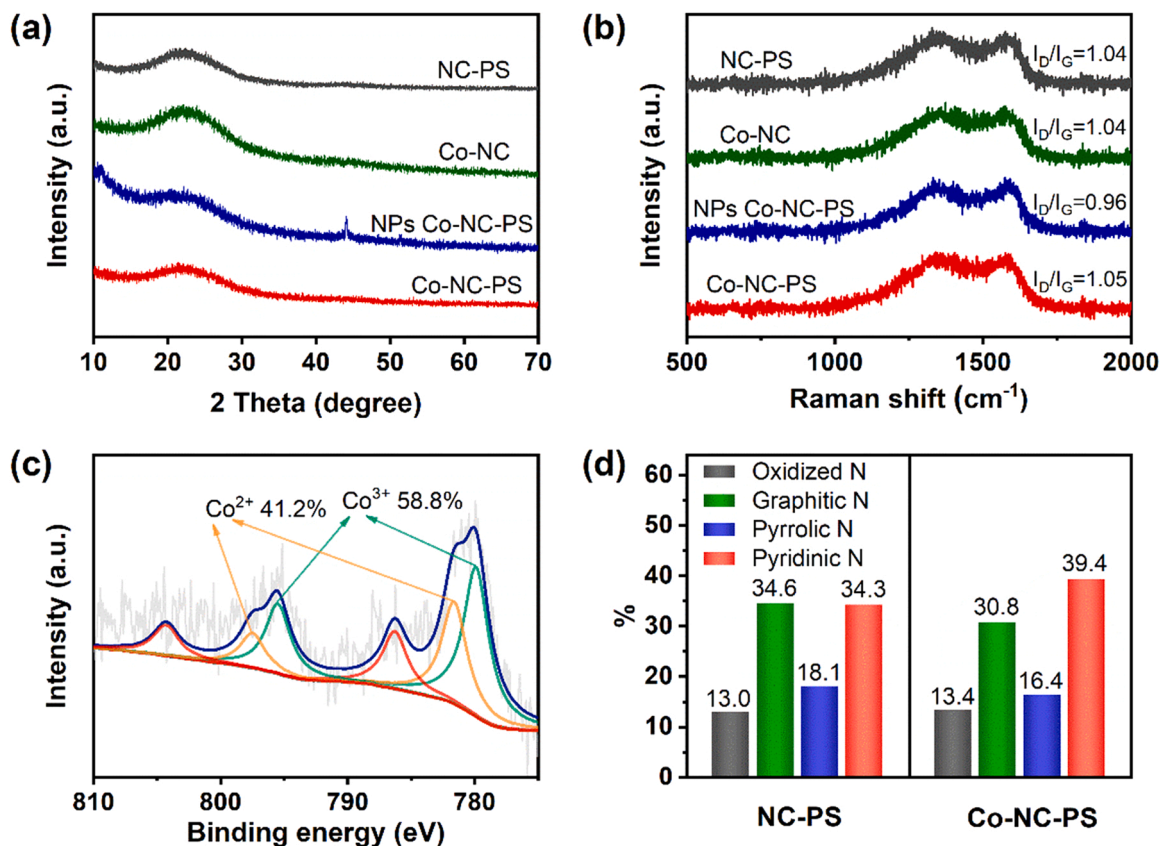

Fig. 2. (a) XRD patterns and (b) Raman spectra of NC-PS, Co-NC, NPs Co-NC-PS and Co-NC-PS, respectively. (c) Co 2p XPS spectrum of Co-NC-PS. (d) The proportions of different N types in NC-PS and Co-NC-PS.
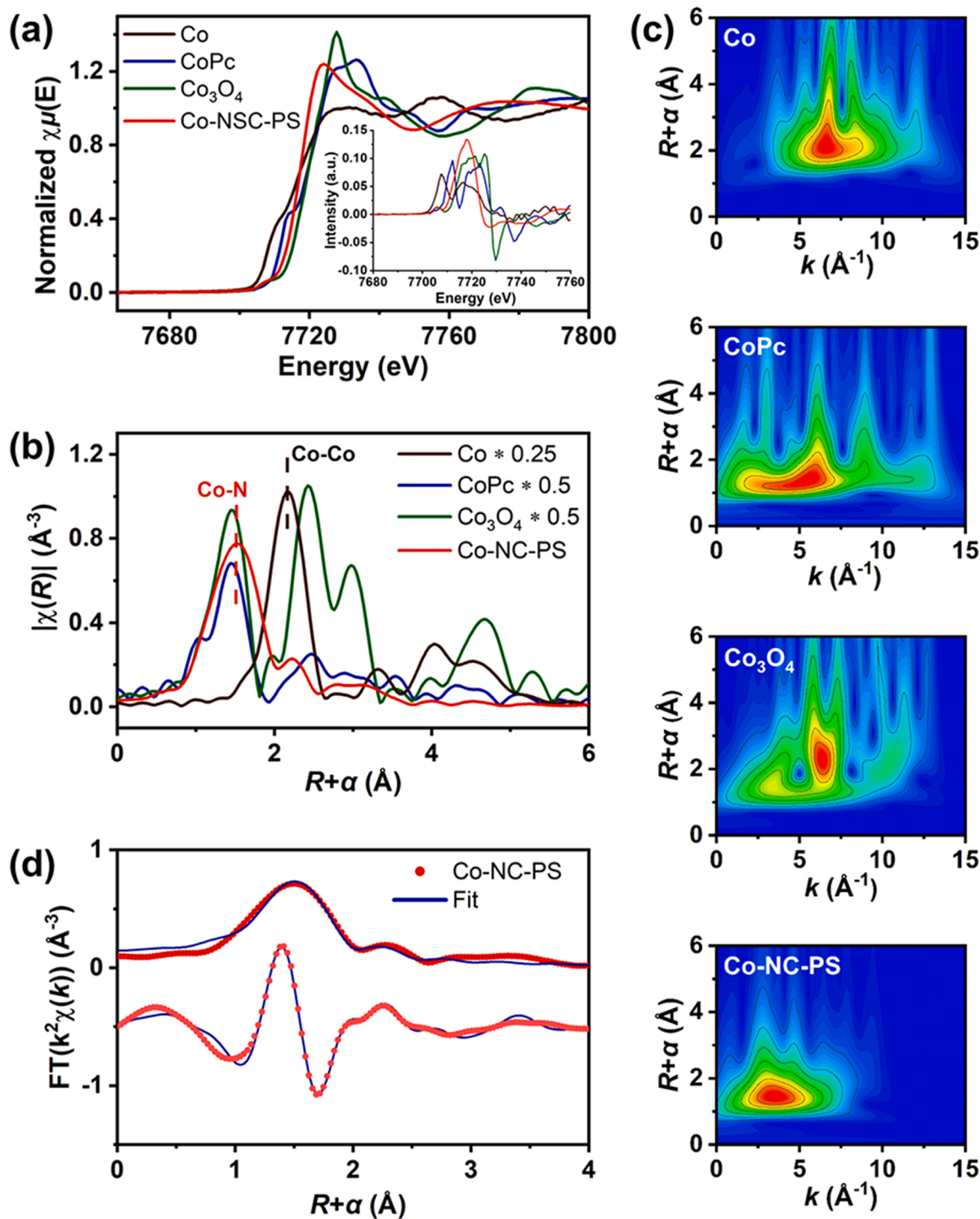
Fig. 3. (a) Normalized XANES spectra at the Co K-edge of Co-NC-PS and reference samples with first derivatives of the XAS data. (b) Non-phase-corrected Fourier-transformed k^2-weighted EXAFS spectra of Co-NC-PS and reference samples. (c) Wavelet transforms of the k^2-weighted EXAFS of Co, CoPc, Co_3O_4 and Co-NC-PS samples. (d) EXAFS and the curve fit for Co-NC-PS are shown in *R*-space (The top and bottom traces are Fourier Transform magnitude and imaginary part, respectively. The data are k^2-weighted and not phase-corrected).

at ~1.50 Å (Fig. 3b), in accordance with the Co−N coordination distance [49]. While a weak peak at ~2.30 Å, close to the Co−Co coordination distance (~2.20 Å), may arise from non-bonded Co−N/C and/or Co−Co single/multiple-scattering paths [50]. In order to determine the attribution of this peak, the wavelet transform (WT) is applied to the Co K-edge EXAFS (Fig. 3c). The WT-EXAFS of Co-NC-PS displays only one intensity maximum in *k*-space and *R*-space at 4.0 Å^{-1} and 1.3 Å,

respectively. By comparing with the reference samples, the *k*-space value is close to the value scattered by light atoms directly coordinated with Co atoms (Co−N/O paths at 3.5 −5.5 Å^{-1}) rather than the Co−Co paths (~7 Å^{-1}). It suggests that the weak peak at ~2.30 Å in *k*-space in FT-EXAFS of Co-NC-PS arises from Co−N rather than Co−Co scattering, consistent with the atomically dispersed Co observed by HAADF-STEM. According to the least-squares EXAFS fitting (Fig. 3d, S8, S9 and

Table S1), the coordination number of Co−N is 4.3 ± 0.6, and the average bond length is 2.01 ± 0.01 Å, indicating that each Co atom coordinates with four N atoms.

3.2. Performance evaluation

Choosing bisphenol A (BPA) as the model pollutant and PMS as the oxidant, the performance of the prepared materials to degrade organic pollutants by activating PMS is studied. As shown in Fig. 4a, without the addition of the catalyst, only PMS can hardly degrade BPA. On the other hand, without PMS, the reduction of BPA is less than 5 % in 60 min. It suggests that the chemical degradation of the BPA is the main decontamination mechanism. To better investigate the catalytic performance, the apparent reaction rate constants (k, min^{-1}) of BPA degradation are obtained by fitting the first-order kinetics. The removal rate of BPA within 60 min is only 60.0 % with NC-PS as the catalyst ($k = 0.031$ min^{-1}), indicating that N-doped carbon contributes little to the activation of PMS (Fig. 4b). Through the preparation of a series of $Co_{(X)}$-NC-PS catalysts with different Co atomic loading, the effect of Co amount on the activation of PMS can be further studied. As shown in Fig. 4b, the $Co_{(1.5)}$-NC-PS, $Co_{(3)}$-NC-PS, $Co_{(12)}$-NC-PS, Co-NC-PS, $Co_{(48)}$-NC-PS and $Co_{(60)}$-NC-PS systems take 60 min, 45 min, 15, min, 10 min, 20 min and 30 min to completely degrade BPA, respectively. The k values are 0.184, 0.628, 0.985, 1.290, 0.751 and 0.562 min^{-1}, respectively (the fitting correlation coefficient R^2 are all above 0.94) (Fig. 4c). The results show that the Co atoms in the Co-NC-PS catalyst may be the main active sites of BPA degradation. The reaction rates of the $Co_{(X)}$-NC-PS systems show a crest shape with the increasing Co precursor dosage and reach up to 1.290 min^{-1} when using Co-NC-PS. Co-NC-PS shows the best catalytic performance, and its reaction rate constant is more than 41 times higher than that of NC-PS. SEM images illustrate that the $Co_{(1.5)}$-NC-PS, $Co_{(3)}$-NC-PS, $Co_{(12)}$-NC-PS, Co-NC-PS, $Co_{(48)}$-NC-PS and $Co_{(60)}$-NC-PS present almost the same three-dimensional ordered macroporous (3DOM) structures with abundant pores after high-temperature calcination (Fig. S10). The increase of Co precursor dosage does not affect the morphology of the material, which excludes the effect of the macroscopic structure of the material on the catalytic activity. XPS survey spectra of the $Co_{(1.5)}$-NC-PS, $Co_{(3)}$-NC-PS, $Co_{(12)}$-NC-PS, Co-NC-PS, $Co_{(48)}$-NC-PS and $Co_{(60)}$-NC-PS show that the Co content is 0.13, 0.17, 0.25, 0.35, 0.50 and 0.56 at%, respectively (Table S2). From $Co_{(1.5)}$-NC-PS to Co-NC-PS, the enhanced activity is attributed to the increment of the Co−N_4 active sites introduced by increasing metal loading amount. However, with the further addition of metal precursors, excessive metal atoms are more likely to aggregate into large-size metal particles [27]. To prove this possibility, the Co 2p XPS spectra of $Co_{(X)}$-NC-PS are further involved (Fig. S11). In Co 2p XPS spectra of the $Co_{(1.5)}$-NC-PS, $Co_{(3)}$-NC-PS, $Co_{(12)}$-NC-PS and Co-NC-PS, no peak assigned to Co^0 could be detected, suggesting that all Co species exist in a dispersed oxidation state. However, with the further increase of Co precursor dosage, a shoulder peak at ~778.5 eV corresponding to the Co^0 appears and gradually strengthens [51]. This result indicates the existence of large-size Co particles, which is confirmed by the TEM images of $Co_{(48)}$-NC-PS and $Co_{(60)}$-NC-PS (Fig. S12a and S12c), revealing granular nanoparticles homogeneously embedded in the carbon skeletons. The clear lattice fringes with interspacing of 0.205 nm illustrated in Fig. S12b and S12d are assigned to the cubic phase Co (111) facet [52]. In summary, it can be concluded that the moderate increase of the Co precursor can increase the Co−N_4 site and improve the catalytic efficiency. However, excessive Co precursor will cause the formation of Co particles, thereby reducing the catalytic efficiency. NPs Co-NC-PS with the same amount of Co source addition is prepared to further demonstrate the role of single-atom Co. With NPs Co-NC-PS as the catalyst, BPA is completely degraded at 60 min (0.306 min^{-1}), indicating that the catalytic efficiency of isolated single-atom Co is higher than that of Co nanoparticles (Fig. S13).

In addition, the effect of the quantity of polystyrene microspheres on BPA degradation is further investigated. With Co-NC and Co-NC-PS (4:1) as the catalyst, the BPA degradation effects are 16.1 % and 95.1 % within 60 min, respectively (Fig. S14). While Co-NC-PS and Co-NC-PS (12:1) systems take only 10 min to degrade BPA completely. The effect of the 3DOM structure on mass transfer efficiency has been explored by customized mass transfer experiments (Table S3). See supporting information for details. The result shows that the 3DOM structure of Co-NC-PS not only fully exposes the active sites but also improves the mass
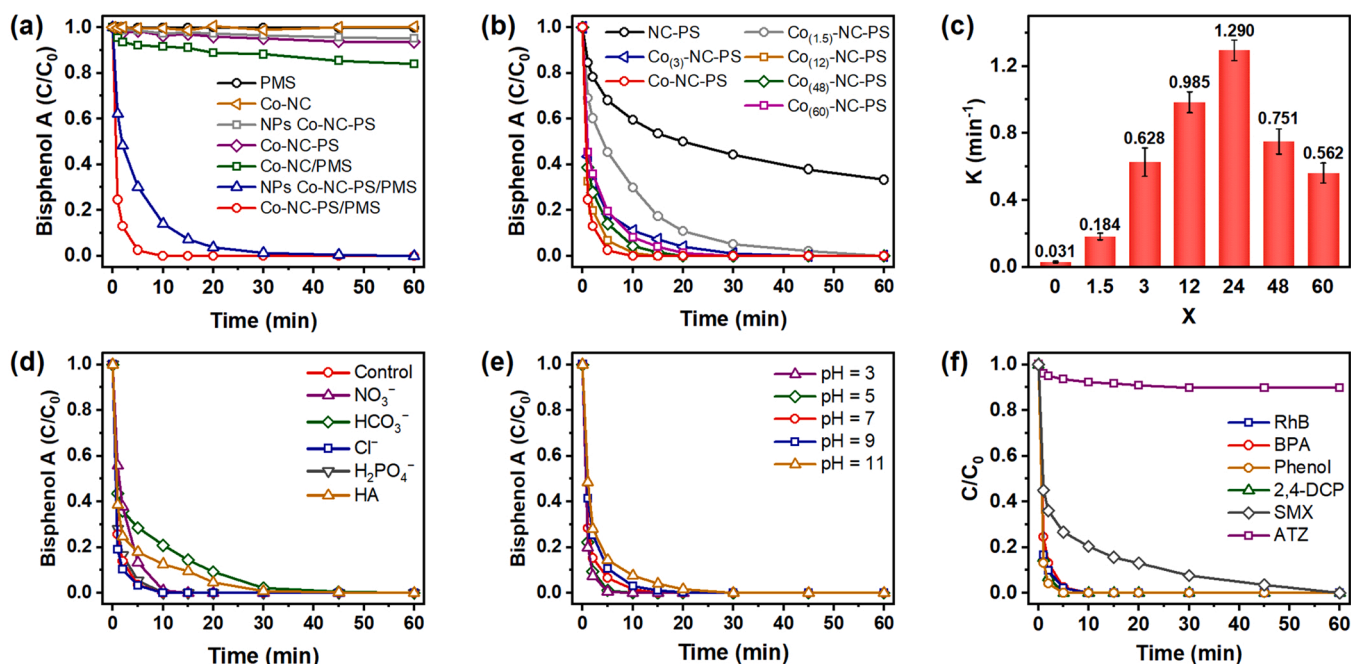

Fig. 4. (a) BPA degradation in different catalysts/PMS systems. (b) BPA degradation in NC-PS and $Co_{(X)}$-NC-PS systems. (c) The pseudo-first order reaction rate constants (k) of NC-PS and $Co_{(X)}$-NC-PS. (d) Effect of 10 mM NO_3^-, 10 mM HCO_3^-, 10 mM Cl^-, 10 mM $H_2PO_4^-$ and 10 mg·L^{-1} HA on the BPA degradation in the Co-NC-PS/PMS system. (e) Effect of pH on the BPA degradation in the Co-NC-PS/PMS system. (f) Degradation of a variety of pollutants in the Co-NC-PS/PMS system.

transfer capacity, which plays a crucial role in improving the catalytic performance. The acceleration of SSA in Co-NC-PS (12:1) is due to the increase of micropores and mesoporous pores caused by the fragmentation of the macroporous structure (Fig. S5h). Herein, with the excessive templates, the 3DOM structure is destroyed. Although the SSA of Co-NC-PS (12:1) is increased, the degradation rate does not increase significantly. Stemming from the economic interest and degradation efficiency consideration, the optimal mass ratio of polystyrene microspheres to the flocculation substrate is 8:1. From the above results, the Co-NC-PS is used in subsequent tests.

The effects of PMS and catalyst dosage on BPA degradation in the representation of Co-NC-PS are also investigated. With the increase of PMS dosage from 100 mg·L^{-1} to 300 mg·L^{-1}, the degradation rate of BPA is significantly increased (Fig. S15a). The k is significantly increased from 0.0315 min^{-1} to 1.290 min^{-1} (Fig. S15b). However, when the PMS dosage increases to 500 mg·L^{-1}, the degradation efficiency does not significantly improve, indicating that the excessive amount of PMS may cause self-quenching in the system and hamper the degradation [53]. As can be seen from the illustration in Fig. S16, the degradation rate of BPA increases significantly as the dosage of Co-NC-PS accelerates from 50 mg·L^{-1} to 150 mg·L^{-1}, indicating that more Co-NC-PS can provide more active sites for PMS activation, and produce more ROSs for BPA degradation. Stemming from the economic interest and degradation efficiency consideration, 100 mg·L^{-1} of catalyst dosage with 300 mg·L^{-1} of PMS dosage is selected as the optimal reaction condition for catalytic activity evaluation.

In addition, considering that there may be a variety of co-existing substances in wastewater, the degradation statuses of BPA by Co-NC-PS catalyst under the existence of various anions (NO$_3^-$, HCO$_3^-$, Cl$^-$ and H$_2$PO$_4^-$) are shown in Fig. 4d. Although such substances could inhibit BPA degradation in a certain extent, BPA can still be completely degraded within 45 min. The inhibiting effect of NO$_3^-$, HCO$_3^-$ and H$_2$PO$_4^-$ on BPA degradation is due to the quenching of the active radicals to form the secondary radicals with lower activity and restrain the BPA oxidation [54]. It is noteworthy that Cl$^-$ can facilitate the degradation of BPA ($k = 1.538$ min^{-1}) on account of a much longer lifetime HOCl may be generated in the Co-NC-PS/PMS/Cl$^-$ system (Fig. S17) [55]. It has been reported that the Co—N$_4$ sites not only act as the essential catalytic sites for PMS activation but also reduce the energy barrier for HOCl formation at a high level of Cl$^-$ [56]. From what has been discussed above, the Co-NC-PS/PMS system has obvious resistance to inorganic anions. To verify the ability of the Co-NC-PS/PMS system to resist macromolecular natural organic matter interference, the effects of different concentrations of humic acid (HA) on the degradation of BPA in the Co-NC-PS/PMS system have been tested. As shown in Fig. 4d and S18, with HA amounts of 10 and 20 mg·L^{-1}, BPA can still be completely degraded at 45 min and 60 min, respectively. BPA degradation may be lightly inhibited by HA owing to its competition with BPA for ROSs during the PMS activation process [57]. The excellent resistance of the Co-NC-PS/PMS system to high HA concentration may be attributed to the 3DOM structure [58]. The average diameter of HA is 783.6 nm, which is much bigger than that of the Co-NC-PS (40 −80 or 160 −200 nm). Co-NC-PS with macropores can intercept the macromolecules, while allowing small molecules to traverse and reach the active sites on the internal channels of Co-NC-PS. Such characteristics, to some extent, can effectively inhibit the competition between HA and BPA on the active sites and the quenching of ROSs, thereby realizing the efficient activation of PMS and degradation of BPA.

The effect of pH on BPA degradation is also investigated. Co-NC-PS has high pH versatility, reaching 100 % BPA removal within 30 min at all investigated pH values from 3 to 11 (Fig. 4e), thus presenting a significant advantage over typical Fenton-like reaction systems. The Co-NC-PS shows better catalytic activity in acidic environments (pH = 3 and 5) than in alkaline environments (pH = 9 and 11). High pH may cause self-decomposition of PMS and hinder its adsorption and activation, thereby slowing the reaction rate [59,60].

The selectivity of degradation of different pollutants is then investigated. Fig. 4f shows the degradation of several organic pollutants in the Co-NC-PS/PMS system. Rhodamine B (RhB), phenol and 2,4-Dichlorophenol (2,4-DCP) could be completely degraded within 10 min, and sulfamethoxazole (SMX) can be completely degraded within 60 min, while atrazine (ATZ) can be degraded by only ~10 % within 60 min. Except for ATZ, the other contaminants can be degraded rapidly, which may be related to the difference in the intramolecular structure of ATZ and the types of free radicals in the system [61]. These results confirm that Co-NC-PS can be used as a catalyst to effectively activate PMS, so as to achieve complete degradation of various dyes and phenolic organic pollutants.

To prove the applicability of the reclamation of the flocculation substrate to prepare the catalyst, the flocculation substrates treated with the four dyes are modified and calcined under the same conditions as that of Co-NC-PS mentioned to obtain Co-NC-PS (Azo Rubine), Co-NC-PS (New Coccine), Co-NC-PS (Orange II) and Co-NC-PS (Brilliant Bule R), respectively. The performances of the prepared materials in the degradation of organic pollutants have been evaluated. As shown in Fig. S19, BPA can be completely degraded within 10 min catalyzed by the Co-NC-PS (Azo Rubine), Co-NC-PS (New Coccine), Co-NC-PS (Orange II) and Co-NC-PS (Brilliant Bule R) systems. These results confirm the applicability of the proposed approach.

Moreover, the stability of the catalyst is further evaluated by reuse tests (Fig. 5a). After the first cycle, the efficiency of NPs Co-NC-PS catalyst decreases by more than 70 % (the blue lines in Fig. 5a). In sharp contrast to the NPs Co-NC-PS catalyst, the Co-NC-PS catalyst shows good recyclability. Although the degradation rate decreased, 97 % BPA can be removed within 60 min after four experimental cycles (the red lines in Fig. 5a). The atomic absorption spectrometer (AAS) is used to detect the amount of cobalt leaching from the solution after the reaction. After the first cycle, the leaching amount of Co in the NPs Co-NC-PS system is 2.2 mg·L^{-1}, while the leaching quantity of Co cannot be detected after the reaction of the Co-NC-PS system. Therefore, it is inferred that the loss of active sites after the reaction may be the main reason for the activity reduction of NPs Co-NC-PS. The strong stability of single-atom Co-NC-PS catalyst most likely originates from the stable Co—N$_4$ active sites.

To disclose the reason for the decline in catalytic performance, cyclic experiments have been carried out without adding BPA under the same other conditions (the recycled catalyst labeled as (Co-NC-PS (used w/o BPA)). XPS results show that the O content of Co-NC-PS increases from 5.98 at% to 11.29 at% after the fourth cycle (Table S2). The proportion of Co^{3+} increases from 58.8 % to 60.9 % while the relative content of pyridine N decreases slightly from 39.4 % to 36.9 %, according to the Co 2p and N 1 s spectra of Co-NC-PS before and after use (Figs. 2c, 5b, S7 and S20, Tables S4 and S5). Furthermore, the C 1 s spectra present the proportion of C−O and C=O increases from 10.0 % and 11.4−11.7 % and 12.3 % after the reaction, respectively. Such results indicate more oxygen-containing groups are introduced into the carbon skeleton during the reaction process (Figs. 5c and 5d). Similarly, the O content in the Co-NC-PS (used w/o BPA) rises to 12.93 %, confirming abundant ROSs attack pollutants and substrate materials indiscriminately [62]. Fourier transform infrared (FTIR) spectroscopy is further employed to characterize the obtained materials. As shown in Fig. 5e, the peaks at 1217 cm^{-1} in the FTIR spectra of the Co-NC-PS (used) and Co-NC-PS (used w/o BPA) are strengthened, corresponding to the infrared band of C–O. This may result from the oxidation of the carbon skeleton by the PMS, which is consistent with the XPS results. In addition, another peak at 1503 cm^{-1} in the FTIR spectrum of the Co-NC-PS (used), corresponding to the skeleton of the benzene ring vibration, appears with the adsorption of the reaction intermediates containing benzene rings. To further verify the reason for catalyst deactivation, the degradation activities of BPA catalyzed by Co-NC-PS (used) and Co-NC-PS (used w/o BPA) have been investigated. With Co-NC-PS (used) and Co-NC-PS (used w/o BPA) as the catalyst, the BPA degradation effects are 79.6 % and
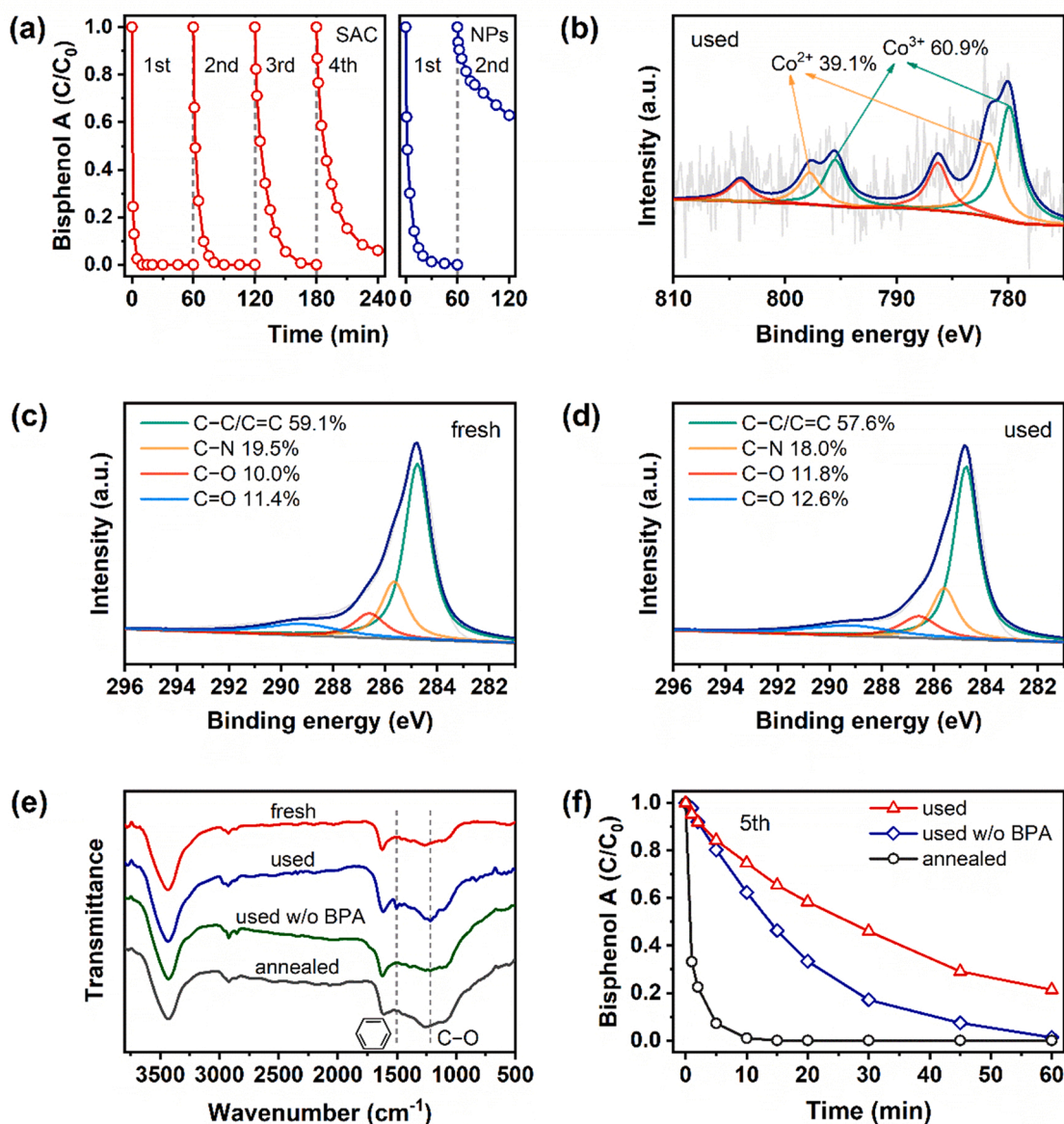
Fig. 5. (a) Stability test of both Co-NC-PS and NPs Co-NC-PS catalysts. (b) Co 2p spectrum of the used Co-NC-PS. C 1 s spectrum of the (c) Co-NC-PS and (d) Co-NC-PS (used). (e) FTIR spectra of the Co-NC-PS, Co-NC-PS (used), Co-NC-PS (used w/o BPA) and Co-NC-PS (annealed). (f) The degradation activities of BPA catalyzed by Co-NC-PS (used), Co-NC-PS (used w/o BPA) and Co-NC-PS (annealed) (the fifth cycle).

98.7 % within 60 min, respectively (Fig. 5f). While Co-NC-PS (used) with lower oxygen content (11.29 %) shows worse activity than Co-NC-PS (used w/o BPA) (O content is 12.93 %). These results indicate that both the oxidation of the carbon skeleton and the adsorption of degradation intermediates lead to the decline of catalytic activity.

Herein, the Co-NC-PS catalyst after the fourth cycle is annealed at 800 ℃ to reduce the catalyst and remove the adsorbed intermediates (the obtained catalyst is named Co-NC-PS (annealed)). The Co-NC-PS (used) and Co-NC-PS (annealed) still maintain the 3DOM structure characterized by SEM, and no significant adsorption of intermediates has been observed in either of them (Fig. S21). The molecular weight of the intermediates may be too small to be observed by SEM, so XPS and FTIR have been used to further characterize the Co-NC-PS (annealed). XPS results show the O content of Co-NC-PS (annealed) decreases to 6.71 % after calcination (Table S2). As shown in Fig. 5e, FTIR spectra show the peaks of the benzene ring and C−O disappear after calcination, verifying that the adsorbed intermediates have been completely removed. In addition, with Co-NC-PS (annealed) as the catalyst, BPA is

completely degraded within 15 min, indicating that the catalytic activity could be restored after calcination (Fig. 5f).

The catalytic stability of Co-NC-PS has been further evaluated by a continuous flow experiment in a fixed bed reactor (Fig. S22). As shown in Fig. S23, 200 mg of catalyst is enough to efficiently purify 9.6 L 20 ppm BPA solution with 100 % removal efficiency in 312 h, implying the satisfactory durability of Co-NC-PS in a long-term oxidation process.

In summary, the oxidation of the carbon skeleton and the adsorption of degradation intermediates lead to the decline of catalytic activity. High-temperature calcination can restore catalytic activity through functional group reduction and adsorbed intermediates removal. The high stability of the Co-NC-PS catalyst is firstly due to the high dispersion of the Co—N_4 sites in the carbon matrix, which reduces the leaching rate of Co. In addition, the stable macropore structure is not easy to be blocked by reaction intermediates in the process of reaction and regeneration, verifying the significance of the 3DOM construction strategy.

3.3. Mechanistic insights into PMS activation

Electron paramagnetic resonance (EPR) analysis and radical quenching experiments are conducted to identify the ROSs generated during PMS activation, in order to investigate the PMS activation mechanism in the Co-NC-PS/PMS system. 5,5-dimethyl-1-pyrroline-N-oxide (DMPO) and 2,2,6,6-tetramethyl-4-piperidone (TEMP) are selected as the spin-trapping agents for the induction of free radicals ($SO_4^{\bullet-}$ and $^{\bullet}OH$) and $^1O_2$, respectively [63]. In the DMPO-trapping EPR experiments, only a very weak signal of the DMPO$-^{\bullet}OH$ is observed in the Co-NC-PS/PMS system, clarifying the inexistence of $SO_4^{\bullet-}$ and a small amount of $^{\bullet}OH$ in the system (Fig. 6a). However, the typical heptet of 5,5-dimethyl-2-pyrrolidone-N-oxyl (DMPOX) adducts (1:2:1:2:1:2:1) appears in the presence of Co-NC-PS (Fig. S24) [64]. Previous studies have shown that DMPO can be oxidized to DMPOX by $^1O_2$ or high-valent metal-oxo species [65,66]. It indicates that $^1O_2$ or high metal oxides may be produced in Co-NC-PS/PMS system. To further clarify the non-radical mechanism, TEMP is then used to trap $^1O_2$ in the system. A characteristic signal of TEMP-$^1O_2$ with the intensity of 1:1:1 appears (Fig. 6b), proving the existence of $^1O_2$. According to the EPR results, it is reasonably speculated that the degradation of BPA by the Co-NC-PS/PMS system mainly depends on active species $^1O_2$ or high-valent metal-oxo species, but not the free radical oxidation.

In order to identify the ROSs generated in the Co-NC-PS/PMS system, radical quenching tests are then conducted (Fig. 6c). MeOH is selected to scavenge $SO_4^{\bullet-}$ and $^{\bullet}OH$ (k (MeOH, $SO_4^{\bullet-}$) = 3.2×10^7 $M^{-1}s^{-1}$, k (MeOH, $^{\bullet}OH$) = 9.7×10^8 $M^{-1}s^{-1}$), as well as TBA is used to selectively quench $^{\bullet}OH$ (k (TBA, $^{\bullet}OH$) = $3.8 - 7.6 \times 10^8$ $M^{-1}s^{-1}$) [67]. Neither MeOH nor TBA shows obvious inhibition even at a 1000-fold molar concentration of PMS. It demonstrates that $SO_4^{\bullet-}$ and $^{\bullet}OH$ are not the main active substances for the oxidation of BPA. Similarly, *p*-Benzoquinone (*p*-BQ) shows a limited quenching effect on $O_2^{\bullet-}$ (k (*p*-BQ, $O_2^{\bullet-}$)
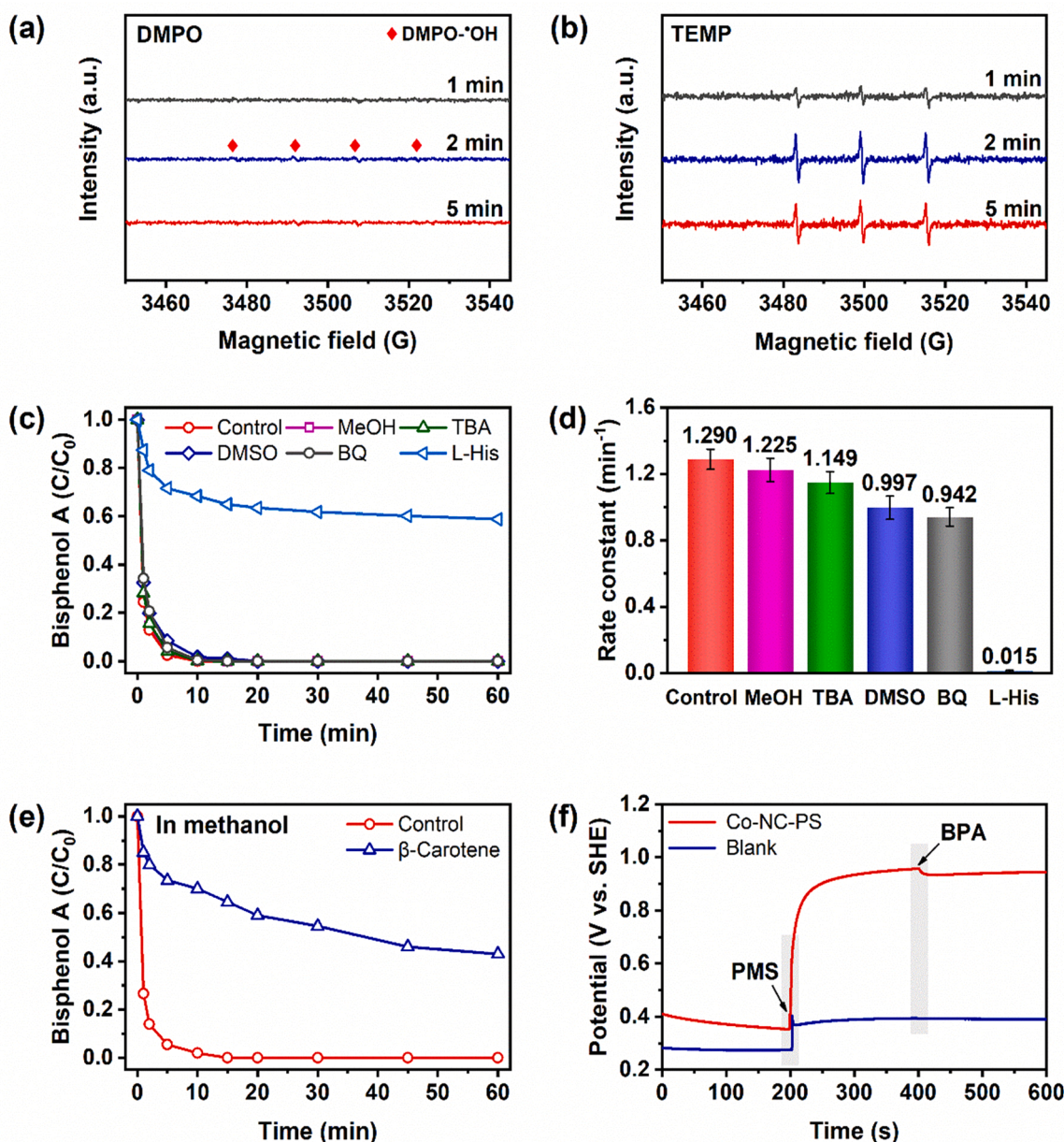

Fig. 6. (a) EPR spectra for $SO_4^{\bullet-}$ and $^{\bullet}OH$ in the presence of DMPO in the Co-NC-PS/PMS system. (b) EPR spectra for $^1O_2$ in the presence of TEMP in the Co-NC-PS/PMS system. (c) The effect of different scavengers on BPA degradation in the Co-NC-PS/PMS system. (d) Pseudo-first order reaction rate comparisons of the Co-NC-PS in different quenching systems. (e) BPA degradation in pure methanol and with the addition of β-Carotene. (f) Open-circuit potential curves of the Co-NC-PS. Reaction conditions: [DMPO] = [TEMP] = 200 mM; MeOH/PMS= TBA/PMS = 1000; [DMSO]= 20 mM; [L-His] = [BQ] = 10 mM; [β-Carotene] = 1.0 mM.

$= 1.0 \times 10^9$ M^{-1} s^{-1}) even in the presence of excessive amounts [68]. Under the above-mentioned conditions, BPA degradation could still be achieved within 15 min. However, when using L-histidine (L-His) as a scavenger for quenching $^1O_2$, the catalytic degradation efficiency of BPA decreases obviously after adding L-His. The k value decreases from 1.290 min^{-1} to 0.015 min^{-1} (Fig. 6d). Such results verify that $^1O_2$ had a significant effect on BPA degradation rather than the SO$_4^{\bullet-}$, $^\bullet$OH or O$_2^{\bullet-}$ radicals, consistent with the EPR results. Nevertheless, it has been reported that many $^1O_2$ scavengers, such as furfuryl alcohol (FFA), L-His and TEMP may react directly with PMS, so the decrease in BPA degradation efficiency may be due to the consumption of PMS by scavengers. β-carotene is another scavenger of $^1O_2$ that may not consume PMS, which is used to further verify the function of $^1O_2$ [69,70]. Since β-carotene is insoluble in water, the radical quenching experiment is performed in the pure methanol system. As methanol inhibits a small amount of SO$_4^{\bullet-}$ and $^\bullet$OH in the solution, the degradation rate of the Co-NC-PS/PMS system in pure methanol is slightly reduced ($k = 1.212$ min^{-1}) (Figs. 6e and S25). However, with the addition of β-carotene, the degradation rate of BPA decreases significantly ($k = 0.021$ min^{-1}), suggesting the major contribution of $^1O_2$ in the Co-NC-PS/PMS system. The result explains the selectivity difference of the Co-NC-PS/PMS system for the degradation of different pollutants. ATZ is difficult to be degraded by $^1O_2$ due to its electron-deficient structure [71]. Surprisingly, when all the possible free ROSs are scavenged out in the BPA solution by adding methanol and β-carotene, the Co-NC-PS/PMS system still removes 58 % BPA, suggesting the BPA degradation process does not solely rely on free ROSs attack.

The high-valent metal-oxo species and direct electron transfer (DET) processes are further investigated. Methyl phenyl sulfoxide (PMSO) can be oxidized by $^1O_2$ or high-valent metal-oxo species to obtain the corresponding oxidation products through the oxygen atom transfer mechanism of methyl phenyl sulfone (PMSO$_2$) [72]. To verify the formation of high-value metal oxides in the Co-NC-PS/PMS system, the consumption of PMSO and the formation of PMSO$_2$ are evaluated by high-performance liquid chromatoid-ultraviolet (HPLC-UV) detection. Without the addition of the catalyst, PMS alone could hardly oxidate PMSO, as only ~5 % of the PMSO is consumed within 60 min (Fig. S26a). Without the addition of BPA, the expenditure of PMSO is only 24.8 % within 60 min, yielding the same amount of PMSO$_2$. The conversion rate of PMSO is much slower than that of the high-valent metal-oxo species-dominated system [73]. With the addition of BPA, the consumption of PMSO is 19.7 %, which may result from the competitive oxidation of PMSO and BPA. However, BPA could be completely degraded within 15 min in the presence of PMSO (Fig. S26b). In addition, DMSO is used as a trap to quench BPA degradation, based on the fact that dimethyl sulfoxide DMSO can be oxidized by high-priced metal oxides. As shown in Figs. 6c and S26c, the degradation rate of BPA slows down slightly as the concentration of DMSO increases from 0 mM to 20 mM. Considering that DMSO can also be oxidized by other reactive oxygen species, it is supposed that high-valent metal-oxo species only have a slight effect on the BPA degradation in the Co-NC-PS/PMS system. Herein, the existence of high-valent metal-oxo species in the degradation system could almost be ruled out. The obvious peak of the DMPOX product in the EPR experiment is mainly caused by the oxidation of DMPO by $^1O_2$ to DMPOX. $^1O_2$ is the main ROS for BPA degradation in the Co-NC-PS/PMS system, which may come from the self-decomposition of PMS rather than the transformation of any free radicals.

Electrochemical techniques are commonly used to study the contribution of DET processes to PMS activation. PMS can be activated by the catalyst to form an active PMS complex that oxidizes organic pollutants directly by electron transfer on the catalyst surface. Fig. 6 f shows the detected open-circuit potential (OCP) of Co-NC-PS loaded on glassy carbon electrodes (GCE) after the continuous addition of PMS and BPA. The open-circuit potential of GCE coated with Co-NC-PS increases immediately after the addition of PMS, owing to the combination of

activated PMS with Co-NC-PS to form catalyst PMS* complex. After the addition of BPA, the OCP slightly decreases due to the reaction between the active PMS complex and BPA. Therefore, the direct electron transfer processes also play a minor role in the degradation of BPA.

Density functional theory (DFT) calculations are employed to further distinguish the different reaction pathways and activation mechanisms of Co active sites. For the transition metal single-atom catalyst, the adsorption or binding of PMS on the catalyst surface facilitates electron transfer between the catalyst and PMS, which is a prerequisite for PMS activation [74]. PMS contains three types of O atoms, one hydroxyl O atom, one peroxy O atom and three terminal O atoms. These three adsorption configurations involving different types of O atoms lead to various PMS activation routes and resultant ROSs generation. Fig. 7a illustrates the intermediate structures of the most likely activation pathway for generating different active species. Pathway I and II: the adsorption with hydroxyl O atom on Co is inclined to generate high metal active species and SO$_4^{\bullet-}$, respectively. Pathway III: the adsorption with peroxy O atom is inclined to generate $^\bullet$OH. Pathway IV: the adsorption with terminal O atoms configuration is more likely to generate $^1O_2$ [75]. For pathway (I), as the electron transfer from metal atoms to PMS, the PMS adsorbed via hydroxyl O undergoes the heterolysis of the bonds around the hydroxyl O atom to form the high-valent metal-oxo structure [76]. And this structure oxidizes organic pollutants through an oxygen atom transfer process. For pathways (II) and (III), the homolysis of the peroxide bond (O—O) leads to the formation of SO$_4^{\bullet-}$ and $^\bullet$OH, respectively, which in turn trigger the degradation reaction. The PMS residues still bound to Co single atoms are released to form SO$_5^{\bullet-}$ with the help of another PMS molecule [29]. For pathway (IV), the formation of $^1O_2$ requires the interaction of two PMS molecules [77], but only the PMS directly linked to the Co—N$_4$ contributes two oxygen atoms. At the same time, the PMS residues are converted to two HSO$_3^-$ [75].

The potential energy profiles of PMS adsorption in these four reaction pathways in the Co-NC-PS/PMS system and corresponding adsorption configurations are shown in Figs. 7b, 7c and S27. In the first step, exothermic adsorption occurred in all three configurations, indicating the spontaneity of the adsorption process and the stability of PMS adsorption to the Co—N$_4$ active site. While the configuration of the terminal O of PMS adsorbed on Co single atoms shows the lowest adsorption energy ($E_{ads} = -2.160$ eV, step1), meaning that it is the most stable adsorption configuration. This adsorption configuration determines that pathway IV is more likely to occur, i.e., it tends to generate $^1O_2$ than other ROSs. Furthermore, in the transformation from *PMS to $^1O_2$, the energy continues to decrease from -2.160 to -3.093 eV (step2) and then to -4.463 eV (step3), verifying that this activation pathway is exergonic and spontaneous. By contrast, the activation pathways I, II and III are only slightly exothermic or even endothermic processes. These results suggest that the Co—N$_4$ active site is more inclined to transform PMS to $^1O_2$ rather than other ROSs, consistent with the results of EPR and inhibition experiment results.

4. Conclusions

In this study, a novel Co single-atom catalyst supported on N-doped three-dimensional ordered microporous (3DOM) carbon (Co-NS-PS) is prepared by a hard-template strategy with the wastewater flocculation substrate as the carbon source. The stable 3DOM structure can boost the mass transfer efficiency and fully expose Co—N$_4$ active sites, thereby enhancing catalytic activity and structural stability. The prepared Co-NS-PS catalyst with highly distributed Co—N$_4$ active sites exhibits splendid Fenton-like catalytic activity (1.290 min^{-1}) and stability for BPA degradation by PMS activation. Based on the quenching experiments and EPR results, $^1O_2$ is proved to be the main functional active specie in this system. Moreover, DFT calculations prove that PMS is more inclined to transform to $^1O_2$ on the Co—N$_4$ active site than other active species. This study provides a novel method for the preparation of
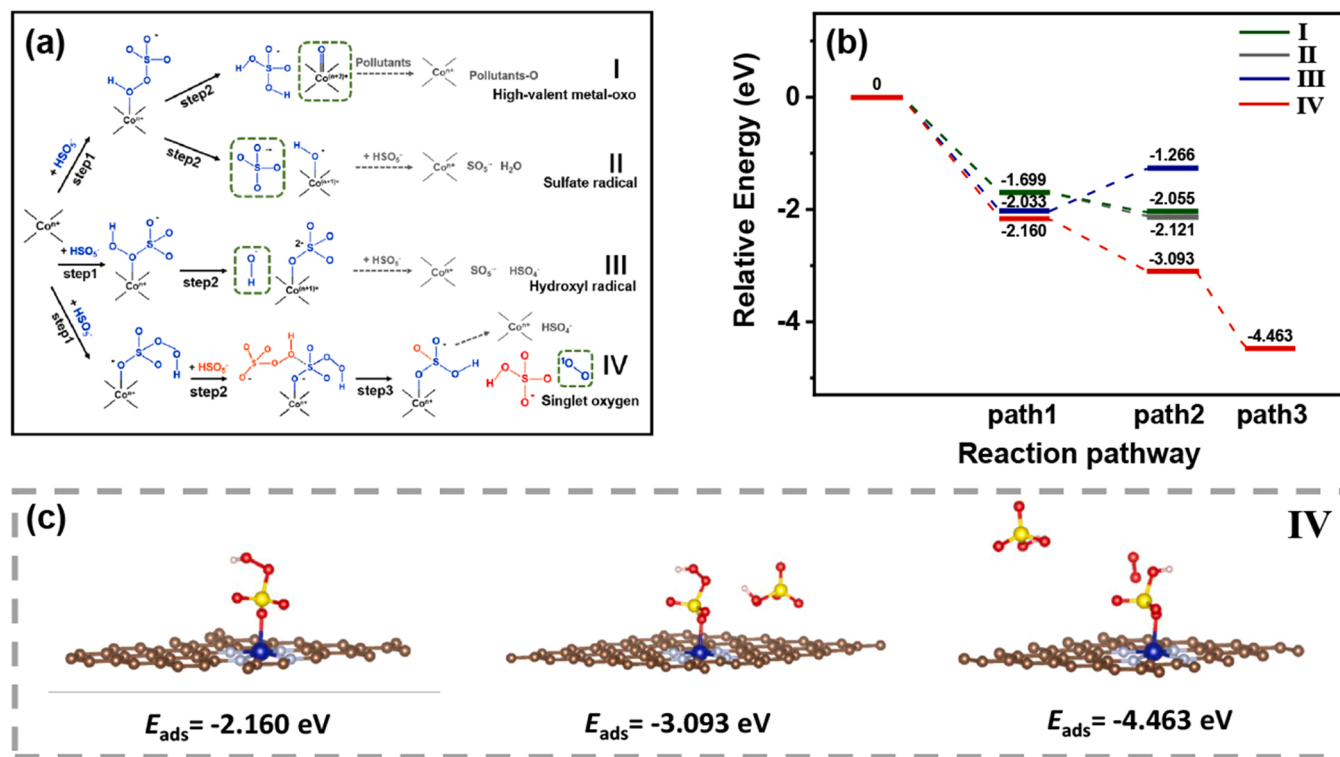
Fig. 7. (a) Pathways for PMS adsorption, activation and generation of high-valent metal-oxo species, $SO_4^{\bullet-}$ radicals, $^{\bullet}OH$ radicals and $^1O_2$ in the Co single-atom system. (b) Potential energy profiles of PMS adsorption for the generation of different active species. (c) Optimized geometric structure of adsorption configuration of PMS for the generation of $^1O_2$ and calculated adsorption energy.

high-value-added products from the recycling of wastes and certain inspirations for the design of novel and efficient SACs for environmental remediation.

CRediT authorship contribution statement

Xu Guo: Conceptualization, Data curation, Methodology, Investigation, Validation, Software, Formal analysis, Visualization, Writing – original draft. **Qicheng Zhang:** Investigation, Formal analysis, Visualization, Writing – original draft. **Hongwei He:** Methodology, Formal analysis. **An Ca:** Investigation, Formal analysis. **Shibo Xi:** Software, Formal analysis. **Jiaqi Du:** Investigation, Formal analysis. **Fengbao Zhang:** Resources. **Xiaobin Fan:** Supervision, Conceptualization, Writing – review & editing, Resources, Funding acquisition. **Wenchao Peng:** Resources, Supervision. **Yang Li:** Resources, Conceptualization, Writing – review & editing, Supervision, Data curation.

Declaration of Competing Interest

The authors declare that they have no known competing financial interests or personal relationships that could have appeared to influence the work reported in this paper.

Data availability

Data will be made available on request.

Acknowledgements

Appendix A. Supporting information

Additional details on the reagents, analytical data, calculation methods, and other associated supplementary texts, figures, and tables. Supplementary data associated with this article can be found in the online version at doi:10.1016/j.apcatb.2023.122886.

References

[1] X. Xiong, I. Yu, L. Cao, D. Tsang, S. Zhang, Y.S. Ok, A review of biochar-based catalysts for chemical synthesis, biofuel production, and pollution control, Bioresour. Technol. 246 (2017) 254–270, https://doi.org/10.1016/j.biortech.2017.06.163.

[2] L. Zhu, J. Ji, J. Liu, S. Mine, M. Matsuoka, J. Zhang, M. Xing, Designing 3D-MoS$_2$ sponge as excellent cocatalysts in advanced oxidation processes for pollutant control, Angew. Chem., Int. Ed. 59 (2020) 13968–13976, https://doi.org/10.1002/anie.202006059.

[3] A. Cl, A. Aa, A. Kdc, A. Bd, B. Nga, A. Gc, B. Sha, A. Vc, Sonophotocatalytic degradation mechanisms of Rhodamine B dye via radicals generation by micro- and nano-particles of ZnO, Appl. Catal. B Environ. 243 (2019) 629–640, https://doi.org/10.1016/j.apcatb.2018.10.078.

[4] X. Li, J. Wang, X. Duan, Y. Li, W. Peng, Fine-tuning radical/nonradical pathways on graphene by porous engineering and doping strategies, ACS Catal. 11 (2021) 4848–4861, https://doi.org/10.1021/acscatal.0c05089.

[5] L. Wu, B. Li, Y. Li, X. Fan, F. Zhang, G. Zhang, Q. Xia, W. Peng, Preferential growth of the cobalt (200) facet in Co@N–C for enhanced performance in a Fenton-like reaction, ACS Catal. 11 (2021) 5532–5543, https://doi.org/10.1021/acscatal.1c00701.

[6] F. Wang, J. Yao, K.E. Sun, B. Xing, Adsorption of dialkyl phthalate esters on carbon nanotubes, Environ. Sci. Technol. 44 (2010) 6985–6991, https://doi.org/10.1021/es101326j.

[7] C. Loderer, A. Worle, W. Fuchs, Influence of different mesh filter module configurations on effluent quality and long-term filtration performance, Environ. Sci. Technol. 46 (2012) 3844–3850, https://doi.org/10.1021/es204636s.

[8] T. Zang, H. Wang, Y. Liu, L. Dai, S. Ai, Fe-doped biochar derived from waste sludge for degradation of Rhodamine B via enhancing activation of peroxymonosulfate, Chemosphere 261 (2020), 127616, https://doi.org/10.1016/j.chemosphere.2020.127616.

[9] X. Duan, C. Su, J. Miao, Y. Zhong, Z. Shao, S. Wang, H. Sun, Insights into perovskite-catalyzed peroxymonosulfate activation: maneuverable cobalt sites for promoted evolution of sulfate radicals, Appl. Catal. B Environ. 220 (2018) 626–634, https://doi.org/10.1016/j.apcatb.2017.08.088.

[10] B.C. Hodges, E.L. Cates, K. Jae-Hong, Challenges and prospects of advanced oxidation water treatment processes using catalytic nanomaterials, Nat. Nanotechnol. 13 (2018) 642–650, https://doi.org/10.1038/s41565-018-0216-x.

[11] Y. Zhou, X. Wang, C. Zhu, D.D. Dionysiou, G. Zhao, G. Fang, D. Zhou, New insight into the mechanism of peroxymonosulfate activation by sulfur-containing minerals: Role of sulfur conversion in sulfate radical generation, Water Res. 142 (2018) 208–216, https://doi.org/10.1016/j.watres.2018.06.002.

[12] S.A. Hakim, S. Jaber, N.Z. Eddine, A. Baalbaki, A. Ghauch, Degradation of theophylline in a UV$_{254}$/PS system: matrix effect and application to a factory effluent, Chem. Eng. J. 380 (2020), 122478, https://doi.org/10.1016/j.cej.2019.122478.

[13] Z. Wei, F.A. Villamena, L.K. Weavers, Kinetics and mechanism of ultrasonic activation of persulfate: an in situ EPR spin trapping study, Environ. Sci. Technol. 51 (2017) 3410–3417, https://doi.org/10.1021/acs.est.6b05392.

[14] H. Wang, W. Guo, B. Liu, Q. Wu, N. Ren, Edge-nitrogenated biochar for efficient peroxydisulfate activation: an electron transfer mechanism, Water Res. 160 (2019) 405–414, https://doi.org/10.1016/j.watres.2019.05.059.

[15] N. Zrinyi, L.T. Pham, Oxidation of benzoic acid by heat-activated persulfate: effect of temperature on transformation pathway and product distribution, Water Res. 120 (2017) 43–51, https://doi.org/10.1016/j.watres.2017.04.066.

[16] Y. Ren, L. Lin, J. Ma, J. Yang, J. Feng, Z. Fan, Sulfate radicals induced from peroxymonosulfate by magnetic ferrospinel MFe$_2$O$_4$ (M = Co, Cu, Mn, and Zn) as heterogeneous catalysts in the water, Appl. Catal. B Environ. 165 (2015) 572–578, https://doi.org/10.1016/j.apcatb.2014.10.051.

[17] B. Li, Y.-F. Wang, L. Zhang, H.-Y. Xu, Enhancement strategies for efficient activation of persulfate by heterogeneous cobalt-containing catalysts: a review, Chemosphere 291 (2022), 132954, https://doi.org/10.1016/j.chemosphere.2021.132954.

[18] G.P. Anipsitakis, D.D. Dionysiou, Radical generation by the interaction of transition metals with common oxidants, Environ. Sci. Technol. 38 (2004) 3705, https://doi.org/10.1021/es035121o.

[19] A.Y. Zhang, Y.Y. He, Y.P. Chen, J.W. Feng, N.H. Huang, F. Lian, Degradation of organic pollutants by Co$_3$O$_4$-mediated peroxymonosulfate oxidation: roles of high-energy {001}-exposed TiO$_2$ support, Chem. Eng. J. 334 (2018) 1430–1439, https://doi.org/10.1016/j.cej.2017.11.078.

[20] H.Q. Sun, C. Kwan, A. Suvorova, H.M. Ang, M.O. Tade, S.B. Wang, Catalytic oxidation of organic pollutants on pristine and surface nitrogen-modified carbon nanotubes with sulfate radicals, Appl. Catal. B Environ. 154 (2014) 134–141, https://doi.org/10.1016/j.apcatb.2014.02.012.

[21] Z. Yang, X.G. Duan, J. Wang, Y. Li, X.B. Fan, F.B. Zhang, G.L. Zhang, W.C. Peng, Facile synthesis of high-performance nitrogen-doped hierarchically porous carbon for catalytic oxidation, ACS Sustain. Chem. Eng. 8 (2020) 4236–4243, https://doi.org/10.1021/acssuschemeng.9b07469.

[22] S. Zhu, X. Huang, F. Ma, L. Wang, X. Duan, S. Wang, Catalytic removal of aqueous contaminants on N-doped graphitic biochars: inherent roles of adsorption and nonradical mechanisms, Environ. Sci. Technol. 52 (2018) 8649–8658, https://doi.org/10.1021/acs.est.8b01817.

[23] Y. Gao, X.G. Duan, K. Li, Q.Q. Jia, Y. Li, X.B. Fan, F.B. Zhang, G.L. Zhang, S. B. Wang, W.C. Peng, Fe containing template derived atomic Fe-N-C to boost Fenton-like reaction and charge migration analysis on highly active Fe-N$_4$ sites, J. Mater. Chem. A 9 (2021) 14793–14805, https://doi.org/10.1039/d1ta02446a.

[24] C. Wang, J. Kim, J. Tang, M. Kim, H. Lim, V. Malgras, J. You, Q. Xu, J. Li, Y. Yamauchi, New strategies for novel MOF-derived carbon materials based on nanoarchitectures, Chem 6 (2020) 19–40, https://doi.org/10.1016/j.chempr.2019.09.005.

[25] Y. Cheng, S.Y. Zhao, B. Johannessen, J.P. Veder, M. Saunders, M.R. Rowles, M. Cheng, C. Liu, M.F. Chisholm, R. De Marco, H.M. Cheng, S.Z. Yang, S.P. Jiang, Atomically dispersed transition metals on carbon nanotubes with ultrahigh loading for selective electrochemical carbon dioxide reduction, Adv. Mater. 30 (2018), e1706287, https://doi.org/10.1002/adma.201706287.

[26] Y.W. Gao, Y. Zhu, T. Li, Z.H. Chen, Q.K. Jiang, Z.Y. Zhao, X.Y. Liang, C. Hu, Unraveling the high-activity origin of single-atom iron catalysts for organic pollutant oxidation via peroxymonosulfate activation, Environ. Sci. Technol. 55 (2021) 8318–8328, https://doi.org/10.1021/acs.est.1c01131.

[27] H. Fei, J. Dong, M.J. Arellano-Jiménez, G. Ye, N. Dong Kim, E.L.G. Samuel, Z. Peng, Z. Zhu, F. Qin, J. Bao, M.J. Yacaman, P.M. Ajayan, D. Chen, J.M. Tour, Atomic cobalt on nitrogen-doped graphene for hydrogen generation, Nat. Commun. 6 (2015) 8668, https://doi.org/10.1038/ncomms9668.

[28] J. Liu, Z. Wei, Z. Gong, M. Yan, Y. Hu, S. Zhao, G. Ye, H. Fei, Single-atom CoN$_4$ sites with elongated bonding induced by phosphorus doping for efficient H$_2$O$_2$ electrosynthesis, Appl. Catal. B Environ. 324 (2023), 122267, https://doi.org/10.1016/j.apcatb.2022.122267.

[29] H.D. Xu, N. Jiang, D. Wang, L.H. Wang, Y.F. Song, Z.Q. Chen, J. Ma, T. Zhang, Improving PMS oxidation of organic pollutants by single cobalt atom catalyst through hybrid radical and non-radical pathways, Appl. Catal. B Environ. 263 (2020), 118350, https://doi.org/10.1016/j.apcatb.2019.118350.

[30] S. Wu, H.B. Liu, G.Y. Lei, H.W. He, J.W. Wu, G.L. Zhang, F.B. Zhang, W.C. Peng, X. B. Fan, Y. Li, Single-atomic iron-nitrogen 2D MOF-originated hierarchically porous carbon catalysts for enhanced oxygen reduction reaction, Chem. Eng. J. 441 (2022), 135849, https://doi.org/10.1016/j.cej.2022.135849.

[31] Y.F. Qi, J. Li, Y.Q. Zhang, Q. Cao, Y.M. Si, Z.R. Wu, M. Akram, X. Xu, Novel lignin-based single atom catalysts as peroxymonosulfate activator for pollutants degradation: role of single cobalt and electron transfer pathway, Appl. Catal. B Environ. 286 (2021), 119910, https://doi.org/10.1016/j.apcatb.2021.119910.

[32] R. Yang, H.J. Li, M. Huang, H. Yang, A.M. Li, A review on chitosan-based flocculants and their applications in water treatment, Water Res. 95 (2016) 59–89, https://doi.org/10.1016/j.watres.2016.02.068.

[33] C. Wan, M.A. Alam, X.Q. Zhao, X.Y. Zhang, S.L. Guo, S.H. Ho, J.S. Chang, F.W. Bai, Current progress and future prospect of microalgal biomass harvest using various flocculation technologies, Bioresour. Technol. 184 (2015) 251–257, https://doi.org/10.1016/j.biortech.2014.11.081.

[34] N. Muhammad, M. Nafees, M.H. Khan, L.Y. Ge, G. Lisak, Effect of biochars on bioaccumulation and human health risks of potentially toxic elements in wheat (Triticum aestivum L.) cultivated on industrially contaminated soil, Environ. Pollut. 260 (2020), 113887, https://doi.org/10.1016/j.envpol.2019.113887.

[35] P.X. Cui, Q. Yang, C. Liu, Y. Wang, G.D. Fang, D.D. Dionysiou, T.L. Wu, Y.Y. Zhou, J.X. Ren, H.B. Hou, Y.J. Wang, An N,S-anchored single-atom catalyst derived from domestic waste for environmental remediation, ACS EST Eng. 1 (2021) 1460–1469, https://doi.org/10.1021/acsestengg.1c00255.

[36] Z. Deng, Z. Jiang, Y. Hu, Y. Liu, L. Zhang, H. Liu, C. Li, 3D ordered macroporous MoS$_2$@C nanostructure for flexible Li-ion batteries, Adv. Mater. 29 (2017), 1603020, https://doi.org/10.1002/adma.201603020.

[37] F. Zhang, T.Y. Liu, M.Y. Li, M.H. Yu, Y. Luo, Y.X. Tong, Y. Li, Multiscale pore network boosts capacitance of carbon electrodes for ultrafast charging, Nano Lett. 17 (2017) 3097–3104, https://doi.org/10.1021/acs.nanolett.7b00533.

[38] P.Q. Yin, T. Yao, Y. Wu, L.R. Zheng, Y. Lin, W. Liu, H.X. Ju, J.F. Zhu, X. Hong, Z. X. Deng, G. Zhou, S.Q. Wei, Y.D. Li, Single cobalt atoms with precise N-coordination as superior oxygen reduction reaction catalysts, Angew. Chem., Int. Ed. 55 (2016) 10800–10805, https://doi.org/10.1002/anie.201604802.

[39] M. Wu, Y. Li, Z. Deng, B.L. Su, Three-dimensionally ordered macroporous titania with structural and photonic effects for enhanced photocatalytic efficiency, ChemSusChem 4 (2011) 1481–1488, https://doi.org/10.1002/cssc.201100082.

[40] H.W. He, Z. Li, K. Li, G.Y. Lei, X.L. Guan, G.L. Zhang, F.B. Zhang, X.B. Fang, W. C. Peng, Y. Li, Bifunctional graphene-based metal-free catalysts for oxidative coupling of amines, ACS Appl. Mater. Interfaces 11 (2019) 31844–31850, https://doi.org/10.1021/acsami.9b08741.

[41] H. He, K. Ma, H. Liu, J. Li, L. Zheng, F. Zhang, X. Fan, W. Peng, J. Ji, Y. Li, Unraveling the amine oxidative coupling activity of hierarchical porous Fe-N$_4$-O$_1$ single-atom catalysts: oxygen atom-mediated dual coordination, J. Mater. Chem. A 10 (2022) 24831–24838, https://doi.org/10.1039/d2ta07198c.

[42] Z.H. Wen, X.C. Wang, S. Mao, Z. Bo, H. Kim, S.M. Cui, G.H. Lu, X.L. Feng, J. H. Chen, Crumpled nitrogen-doped graphene nanosheets with ultrahigh pore volume for high-performance supercapacitor, Adv. Mater. 24 (2012) 5610–5616, https://doi.org/10.1002/adma.201201920.

[43] X.Y. Liu, H.R. Yu, J.H. Ji, Z. Chen, M.X. Ran, J.L. Zhang, M.Y. Xing, Graphene oxide-supported three-dimensional cobalt-nickel bimetallic sponge-mediated peroxymonosulfate activation for phenol degradation, ACS EST Eng. 1 (2021) 1705–1714, https://doi.org/10.1021/acsestengg.1c00307.

[44] A. Cai, H.W. He, Q.C. Zhang, Y.S. Xu, X.T. Li, F.B. Zhang, X.B. Fan, W.C. Peng, Y. Li, Synergistic effect of N-doped sp^2 carbon and porous structure in graphene gels toward selective oxidation of C-H bond, ACS Appl. Mater. Interfaces 13 (2021) 13087–13096, https://doi.org/10.1021/acsami.0c21177.

[45] H. Zhou, S. Hong, H. Zhang, Y.T. Chen, H.H. Xu, X.K. Wang, Z. Jiang, S.L. Chen, Y. Liu, Toward biomass-based single-atom catalysts and plastics: highly active single-atom Co on N-doped carbon for oxidative esterification of primary alcohols, Appl. Catal. B Environ. 256 (2019), https://doi.org/10.1016/j.apcatb.2019.117767.

[46] Z.P. Zeng, L.Y. Gan, H.B. Yang, X.Z. Su, J.J. Gao, W. Liu, H. Matsumoto, J. Gong, J. M. Zhang, W.Z. Cai, Z.Y. Zhang, Y.B. Yan, B. Liu, P. Chen, Orbital coupling of hetero-diatomic nickel-iron site for bifunctional electrocatalysis of CO$_2$ reduction and oxygen evolution, Nat. Commun. 12 (2021), https://doi.org/10.1038/s41467-021-24052-5.

[47] L. Zu, X. Qian, S. Zhao, Q. Liang, Y.E. Chen, M. Liu, B.-J. Su, K.-H. Wu, L. Qu, L. Duan, H. Zhan, J.-Y. Zhang, L. Li, J.Y. Juang, J. Zhu, D. Li, A. Yu, D. Zhao, Self-assembly of Ir-based nanosheets with ordered interlayer space for enhanced electrocatalytic water oxidation, J. Am. Chem. Soc. 144 (2022) 2208–2217, https://doi.org/10.1021/jacs.1c11241.

[48] C.H. Chu, J. Yang, X.C. Zhou, D.H. Huang, H.F. Qi, S. Weon, J.F. Li, M. Elimelech, A.Q. Wang, J.H. Kim, Cobalt single atoms on tetrapyridomacrocyclic support for efficient peroxymonosulfate activation, Environ. Sci. Technol. 55 (2021) 1242–1250, https://doi.org/10.1021/acs.est.0c06086.

[49] W. Sun, L. Du, Q. Tan, J.G. Zhou, Y.F. Hu, C.Y. Du, Y.Z. Gao, G.P. Yin, Engineering of nitrogen coordinated single cobalt atom moieties for oxygen electroreduction, ACS Appl. Mater. Interfaces 11 (2019) 41258–41266, https://doi.org/10.1021/acsami.9b11830.

[50] G. Rossi, F. d'Acapito, L. Amidani, F. Boscherini, M. Pedio, Local environment of metal ions in phthalocyanines: K-edge X-ray absorption spectra, Phys. Chem. Chem. Phys. 18 (2016) 23686–23694, https://doi.org/10.1039/c6cp04022e.

[51] Y. Liu, X.Y. Chen, Y.L. Yang, Y. Feng, D.L. Wu, S. Mao, Activation of persulfate with metal-organic framework-derived nitrogen-doped porous Co@C nanoboxes for highly efficient p-Chloroaniline removal, Chem. Eng. J. 358 (2019) 408–418, https://doi.org/10.1016/j.cej.2018.10.012.

[52] S.Y. Zhang, L. Wang, T.Z. Xie, Q.M. Chen, W.C. Peng, Y. Li, F.B. Zhang, X.B. Fan, Heterointerface enhanced NiFe LDH/V-Co$_4$N electrocatalysts for the oxygen evolution reaction, J. Mater. Chem. A 10 (2022) 21523–21530, https://doi.org/10.1039/d2ta04120k.

[53] X.G. Duan, C. Su, L. Zhou, H.Q. Sun, A. Suvorova, T. Odedairo, Z.H. Zhu, Z.P. Shao, S.B. Wang, Surface controlled generation of reactive radicals from persulfate by carbocatalysis on nanodiamonds, Appl. Catal. B Environ. 194 (2016) 7–15, https://doi.org/10.1016/j.apcatb.2016.04.043.

[54] J.C.E. Yang, Y. Lin, H.H. Peng, B.L. Yuan, D.D. Dionysiou, X.D. Huang, D.D. Zhang, M.L. Fu, Novel magnetic rod-like Mn-Fe oxycarbide toward peroxymonosulfate activation for efficient oxidation of butyl paraben: radical oxidation versus singlet oxygenation, Appl. Catal. B Environ. 268 (2020), 118549, https://doi.org/10.1016/j.apcatb.2019.118549.

[55] J.L. Wang, S.Z. Wang, Effect of inorganic anions on the performance of advanced oxidation processes for degradation of organic contaminants, Chem. Eng. J. 411 (2021), 128392, https://doi.org/10.1016/j.cej.2020.128392.

[56] L.J. Peng, Y.N. Shang, B.Y. Gao, X. Xu, Co_3O_4 anchored in N, S heteroatom co-doped porous carbons for degradation of organic contaminant: role of pyridinic N-Co binding and high tolerance of chloride, Appl. Catal. B Environ. 282 (2021), 119484, https://doi.org/10.1016/j.apcatb.2020.119484.

[57] H.C. Li, C. Shan, B.C. Pan, Fe(III)-doped g-C_3N_4 mediated peroxymonosulfate activation for selective degradation of phenolic compounds via high-valent iron-oxo species, Environ. Sci. Technol. 52 (2018) 2197–2205, https://doi.org/10.1021/acs.est.7b05563.

[58] J. Liang, R. Chen, J.-n Gu, J. Li, F. Shi, Y. Xue, B. Huang, M. Guo, J. Jia, K. Li, T. Sun, Selective and efficient removal of emerging contaminants by sponge-like manganese ferrite synthesized using a solvent-free method: crucial role of the three-dimensional porous structure, Water Res. 232 (2023), 119685, https://doi.org/10.1016/j.watres.2023.119685.

[59] W. Ren, G. Nie, P. Zhou, H. Zhang, X.G. Duan, S.B. Wang, The intrinsic nature of persulfate activation and N-doping in carbocatalysis, Environ. Sci. Technol. 54 (2020) 6438–6447, https://doi.org/10.1021/acs.est.0c01161.

[60] P.J. Duan, Y.F. Qi, S.S. Feng, X.M. Peng, W. Wang, Y. Yue, Y. Shang, Y.W. Li, B. Y. Gao, X. Xu, Enhanced degradation of clothianidin in peroxymonosulfate/catalyst system via core-shell FeMn@N-C and phosphate surrounding, Appl. Catal. B Environ. 267 (2020), 118717, https://doi.org/10.1016/j.apcatb.2020.118717.

[61] B. Li, B. Ma, M.Y. Wei, Y. Li, X.B. Fan, F.B. Zhang, G.L. Zhang, Q. Xia, W.C. Peng, Synthesis of Co-NC catalysts from spent lithium-ion batteries for Fenton-like reaction: generation of singlet oxygen with ~100% selectivity, Carbon 197 (2022) 76–86, https://doi.org/10.1016/j.carbon.2022.06.029.

[62] Y.N. Shang, X. Xu, B.Y. Gao, S.B. Wang, X.G. Duan, Single-atom catalysis in advanced oxidation processes for environmental remediation, Chem. Soc. Rev. 50 (2021) 5281–5322, https://doi.org/10.1039/d0cs01032d.

[63] Y. Zhao, D. Wu, Y. Chen, Y. Li, X.B. Fan, F.B. Zhang, G.L. Zhang, W.C. Peng, Thermal removal of partial nitrogen atoms in N-doped graphene for enhanced catalytic oxidation, J. Colloid Interface Sci. 585 (2021) 640–648, https://doi.org/10.1016/j.jcis.2020.10.043.

[64] H.Z. Wang, W.Q. Guo, B.H. Liu, Q.L. Wu, H.C. Luo, Q. Zhao, Q.S. Si, F. Sseguya, N. Q. Ren, Edge-nitrogenated biochar for efficient peroxydisulfate activation: an electron transfer mechanism, Water Res. 160 (2019) 405–414, https://doi.org/10.1016/j.watres.2019.05.059.

[65] N. Jiang, H.D. Xu, L.H. Wang, J. Jiang, T. Zhang, Nonradical oxidation of pollutants with single-atom-Fe(III)-activated persulfate: Fe(V) being the possible intermediate oxidant, Environ. Sci. Technol. 54 (2020) 14057–14065, https://doi.org/10.1021/acs.est.0c04867.

[66] X.N. Li, X. Huang, S.B. Xi, S. Miao, J. Ding, W.Z. Cai, S. Liu, X.L. Yang, H.B. Yang, J. J. Gao, J.H. Wang, Y.Q. Huang, T. Zhang, B. Liu, Single cobalt atoms anchored on porous N-doped graphene with dual reaction sites for efficient Fenton-like catalysis, J. Am. Chem. Soc. 140 (2018) 12469–12475, https://doi.org/10.1021/jacs.8b05992.

[67] Y. Zhou, J. Jiang, Y. Gao, J. Ma, S.Y. Pang, J. Li, X.T. Lu, L.P. Yuan, Activation of peroxymonosulfate by benzoquinone: a novel nonradical oxidation process, Environ. Sci. Technol. 49 (2015) 12941–12950, https://doi.org/10.1021/acs.est.5b03595.

[68] P. Eyer, Effects of superoxide dismutase on the autoxidation of 1,4-hydroquinone, Chem. Biol. Interact. 80 (1991) 159–176, https://doi.org/10.1016/0009-2797(91)90022-y.

[69] J.J. You, C.Y. Zhang, Z.L. Wu, Z.M. Ao, W.Y. Sun, Z.K. Xiong, S.J. Su, G. Yao, B. Lai, N-doped graphite encapsulated metal nanoparticles catalyst for removal of Bisphenol A via activation of peroxymonosulfate: a singlet oxygen-dominated oxidation process, Chem. Eng. J. 415 (2021), 128890, https://doi.org/10.1016/j.cej.2021.128890.

[70] X.M. Liu, J. Wang, D. Wu, Z. Wang, Y. Li, X.B. Fan, F.B. Zhang, G.L. Zhang, W. C. Peng, N-doped carbon dots decorated 3D g-C_3N_4 for visible-light driven peroxydisulfate activation: insights of non-radical route induced by Na^+ plus doping, Appl. Catal. B Environ. 310 (2022), 121304, https://doi.org/10.1016/j.apcatb.2022.121304.

[71] J.J. He, Y. Wan, W.J. Zhou, ZIF-8 derived Fe-N coordination moieties anchored carbon nanocubes for efficient peroxymonosulfate activation via non-radical pathways: role of FeN_x sites, J. Hazard. Mater. 405 (2021), 124199, https://doi.org/10.1016/j.jhazmat.2020.124199.

[72] B.K. Huang, Z.K. Xiong, P. Zhou, H. Zhang, Z.C. Pan, G. Yao, B. Lai, Ultrafast degradation of contaminants in a trace cobalt(II) activated peroxymonosulfate process triggered through borate: indispensable role of intermediate complex, J. Hazard. Mater. 424 (2022), 127641, https://doi.org/10.1016/j.jhazmat.2021.127641.

[73] B.H. Liu, W.Q. Guo, Q.S. Si, W.R. Jia, S.S. Zheng, H.Z. Wang, Q. Zhao, H.C. Luo, J. Jiang, N.Q. Ren, Atomically dispersed cobalt on carbon nitride for peroxymonosulfate activation: switchable catalysis enabled by light irradiation, Chem. Eng. J. 446 (2022), 137277, https://doi.org/10.1016/j.cej.2022.137277.

[74] J. Lee, U. von Gunten, J.H. Kim, Persulfate-based advanced oxidation: critical assessment of opportunities and roadblocks, Environ. Sci. Technol. 54 (2020) 3064–3081, https://doi.org/10.1021/acs.est.9b07082.

[75] J.H. Hu, Y. Li, Y.B. Zou, L. Lin, B. Li, X.Y. Li, Transition metal single-atom embedded on N-doped carbon as a catalyst for peroxymonosulfate activation: a DFT study, Chem. Eng. J. 437 (2022), 135428, https://doi.org/10.1016/j.cej.2022.135428.

[76] K. Qian, H. Chen, W.L. Li, Z.M. Ao, Y.N. Wu, X.H. Guan, Single-atom Fe catalyst outperforms its homogeneous counterpart for activating peroxymonosulfate to achieve effective degradation of organic contaminants, Environ. Sci. Technol. 55 (2021) 7034–7043, https://doi.org/10.1021/acs.est.0c08805.

[77] W. Miao, Y. Liu, D.D. Wang, N.J. Du, Z.W. Ye, Y. Hou, S. Mao, K. Ostrikov, The role of Fe-N_x single-atom catalytic sites in peroxymonosulfate activation: formation of surface-activated complex and non-radical pathways, Chem. Eng. J. 423 (2021), 130250, https://doi.org/10.1016/j.cej.2021.130250.